

# A Multiharvested Self-Powered System in a Low-Voltage Low-Power Technology

J. Colomer-Farrarons, *Student Member, IEEE*, P. Miribel-Català, *Member, IEEE*,  
A. Saiz-Vela, *Student Member, IEEE*, and J. Samitier, *Member, IEEE*

**Abstract**—A multiharvesting system conception focused on low-voltage (up to 2.5 V) and low-power applications is presented and validated as a point-of-view system. Using just this application-specified integrated circuit, with a total quiescent power consumption of 160  $\mu\text{W}$ , the harvesting system is able to collect and manage energy from different power sources, such as solar light (indoor environment), vibration (low-voltage piezoelectric generators), and electromagnetic induction (operating with a carrier frequency of 13.56-MHz regulated band). The maximum total power harvested with the addition of the three harvesting sources is around 6.4 mW, for the operating conditions defined by a PZT at 7  $\text{m/s}^2$  at 80 Hz, 1500 lx for a laboratory illumination, and 200 mW emitted by a base transmitter at 25-mm distance between coils. A broad and detailed description of all low-power-consumption circuits involved in the multiharvesting system is described, emphasizing their design for low-voltage and low-power applications.

**Index Terms**—Electric power generation, energy scavenging, low-power electronics, power conditioning.

## I. INTRODUCTION

THE first energy cell, the battery, was invented by Alessandro Volta in 1799. His invention predated the first mechanical-to-electrical energy converter device discovered by Michael Faraday. At the beginning, batteries were the only way to generate electrical energy. It was at the end of the 19th century when electricity was brought to cities by wires, while battery use was relegated to mobile platforms.

Battery technology has undergone tremendous progress since it was first discovered. This progress has enabled the explosion of a wide range of new applications such as in mobile devices. However, new trends in technology added to some intrinsic limitations of batteries have motivated research into new energy generation solutions [1]–[3].

There is a great interest in using free available external energy sources for powering small electronic systems, a process known as energy harvesting [4]. We must distinguish between macro and micro energy-harvesting scales. Macroharvesting is related to energy recovery in the range from kilowatts to megawatts, which are fed to the grid. From the microscale point of view, a limited amount of energy, in the range from

nanowatts to milliwatts, can be obtained from different types of external ambient sources and energy transducers [5]–[8], like vibrations [9]–[13], heat [14]–[17], light [18]–[20], radio waves [21], [22], or from human activity [23]–[26]. Estimates of the available energy per unit area, or volume, for each harvesting source, are reported in Table I. These values depend heavily on the excitation conditions and technologies used. From these different types of power sources and harvesting solutions, it is possible to recover a peak power of 400  $\mu\text{W}$  for mechanical-to-electrical harvesting based on piezoelectric microelectromechanical systems (MEMS), operating at 1 kHz and generating voltages below 1 V [9] for optimal load conditions, or, as in [10], based on micropower generators based on a laminate piezoelectric membrane, generating 22  $\mu\text{W}$  of power and peak voltages up to 2.45 V with no load. Following the objective to design energy-harvesting devices based on MEMS solutions, an electrostatic microgenerator is presented in [10]. In this case, a mechanical-to-electrical conversion based on an electrostatic solution instead of a piezoelectric or electromagnetic solution, the peak voltage generated can be up to 65 V, and discrete electronics are used. This type of solution imposes some high-voltage technology like the i2T100 Europractice [27]. In [12], a piezoelectric cantilever working at lower frequencies of operation (65 Hz), generating higher voltages (up to 15 V) and a maximum power of 350  $\mu\text{W}$ , is presented. An interesting point of progress is shown in [25], because two power sources are combined: piezoelectric and permanent magnetic energy scavenging. These elements are discrete, and the total power theoretically generated is 44 mW: 37 mW from the electromagnetic source and 6 mW from the piezoelectric source. In [18], the utilization of indoor cells for extremely low conditions of illumination, and low voltages of operation, is shown for a cell of 55 mm  $\times$  20 mm  $\times$  1.1 mm with a power of 5  $\mu\text{W}$  at 10 lx to 200  $\mu\text{W}$  at 1450 lx for a voltage drop of 2 V.

Looking for a microharvested solution of cubic centimeter of volume, which defines a smart multi-self-powered device for measurements, monitoring, and communications, this would be limited by area and volume. In this way, the combination of several harvesting sources is mandatory. The combination of three sources, namely, light, radio frequency (RF), and vibration, in the range of low voltages (operative from 1.2 to 2.5 V), which are based on indoor illumination, typically 100  $\mu\text{W}/\text{cm}^2$  in an illuminated office, inductive coupling, and vibrational generators, is presented in this paper.

Nowadays, there has been more information related to the harvesting topic and its impact on the green-house actuations.

Manuscript received February 10, 2010; revised July 7, 2010; accepted October 23, 2010. Date of publication November 29, 2010; date of current version August 12, 2011.

The authors are with the SIC-BIO: Bioelectronics and Nanobioengineering Laboratory, Department of Electronics, Faculty of Physics, University of Barcelona, 08028 Barcelona, Spain (e-mail: jcolomer@el.ub.es; pmiribel@el.ub.es; asaiz@el.ub.es; samitier@el.ub.es).

Color versions of one or more of the figures in this paper are available online at <http://ieeexplore.ieee.org>.

Digital Object Identifier 10.1109/TIE.2010.2095395

TABLE I  
ENERGY-HARVESTING ESTIMATIONS

Energy Source	Performance	
<b>Ambient Light</b>	Indoor $10\mu\text{W}/\text{cm}^2$ (low illumination) Typical office $100\mu\text{W}/\text{cm}^2$ Outdoor $10\text{mW}/\text{cm}^2$ Full bright sun $10\text{mW}/\text{cm}^2$	Solar cells ( $6830\text{ lx } 10\text{W}/\text{m}^2$ ) Indoor solar cells (10lx to 1400 lx)
<b>Vibrational</b>	$4\mu\text{W}/\text{cm}^3$ (human motion Hz range) $800\mu\text{W}/\text{cm}^3$ (machines-kHz ranges) These numbers depend heavily on size, excitations, technologies, etc. Typically: Piezoelectric $\sim 200\mu\text{W}/\text{cm}^3$ Electrostatic $\sim 50\text{-}100\mu\text{W}/\text{cm}^3$ Electromagnetic $< 1\mu\text{W}/\text{cm}^3$	[5][7] Microgenerators $350\mu\text{W}$ [12] $22\mu\text{W}$ [10] $400\mu\text{W}$ [9]
<b>RF</b>	GSM $4\mu\text{W}/\text{cm}^2$ WiFi $0.001\text{mW}/\text{cm}^2$ These numbers depend heavily on frequency of operation and distance between base station and receiver.	$< 1\mu\text{W}/\text{cm}^2$ unless near a transmitter [6] $\approx 1\text{mW}$ for proximate stations (inductive coils) @900MHz, 1.1meter @ 24.98dBm ( $0.315\text{W}$ ), $\sim 20\mu\text{W}$ [48] @4MHz, 25mm (subcutaneous powering) $>5\text{mW}$ [62]
<b>Temperature Difference</b>	Human $25\mu\text{W}/\text{cm}^2$ - $60\mu\text{W}/\text{cm}^2$ Industry $10\text{mW}/\text{cm}^2$	Thermoelectric generators $60\mu\text{W}/\text{cm}^2$ Thermolife® $\Delta T=5^\circ\text{C}$ . [7][14][48]

In [www.EETimes.com](http://www.EETimes.com), there is a reference to sustainable buildings based on energy harvesting [28] related to EnOcean GmbH [29], a spin-off from Siemens, and interest in combining energy-harvesting circuits with RF modules, in order to define self-powered sensor networks [30] and monitor energy harvesting from natural motion [32].

There is also interest in monitoring the integrity of transport infrastructures like bridges [33] and commercial solutions like MicroStrain (Williston, VT) [34], Midé Engineering Smart Technologies (Cambridge and Boston, MA) [35], or Perpetuum (spin-off from the University of Southampton, U.K.) [36]. Another example is the CC430 technology platform by Texas Instruments [37]. This platform helps the design of advanced applications such as RF networking, energy harvesting, industrial monitoring and tamper detection, personal wireless networks, and automatic metering infrastructure.

The advances in semiconductor technologies related to the reduction of the transistor’s size allow the industry to obtain more interest in the development of new self-powered portable electronic devices that incorporate a great variety of circuitry and functions [38]–[40].

Energy harvesting, small-format batteries, and power management integrated circuits (ICs) are technologies that will enable commercialization of the next generation of ultralow-power electronic devices and systems. Such devices are being deployed for wireless as well as wired systems such as mesh networks [41], [42], sensor and control systems, RF identification (RFID) devices, MEMS [43]–[45], and so forth. Some interesting work has been reported in the field of power harvesting relating to passive wireless microsensors operating in the range of ultrahigh frequency, in the ISM 900-MHz and GHz bands, defining a far-field coupling, where the power is

supplied via a wireless base station. In the U.S., the maximum power delivered by the base station cannot exceed 4 W, defining a far-field coupling of just a few meters. Such systems are based on circuits that rectify and set up the induced voltage across the integrated antenna, which is a low voltage on the order of hundreds of millivolts, in function of the distance between the base and the tag. Such circuits are known as micropower rectifiers, as derived in [46]–[48]. Efforts have been made to improve the efficiency of such RF/dc rectifier/multiplier circuits. In [49], for instance, the authors developed a CMOS solution implemented in a  $0.18\text{-}\mu\text{m}$  technology, operating with an input carrier of 900 MHz, with an input voltage of 250 mV in the integrated antenna in the tag, which will theoretically generate an average power of  $25\mu\text{W}$ , with an output voltage of 1.8 V to supply the tag electronics.

The reduced battery maintenance and replacement are expected to provide substantial growth market opportunities for power management technologies. Overall, the commercial viability and market opportunities, the dissemination and adoption of new value-added technologies based on energy harvesting, contribute to a global green growth exploiting new market and technological challenges.

In application areas as diverse as aircraft construction, personal health care monitoring systems, or burglary detection systems, energy harvesting is on the verge of developing a market with a multibillion-dollar potential. For example, an electronic device including a semiconductor-based thermoelectric generator (TEG), which transforms temperature gradient into electrical energy, could be worn on the body using human body heat as an energy source for medical monitoring [50]–[52], delivering a power of 0.2–0.3 mW at  $22^\circ\text{C}$ . Furthermore, the total amount of energy demanded by the energy suppliers could

be greatly reduced just by walking around while carrying on the body or clothes several autonomous portable devices in which energy harvesting from vibrations has been included. The benefits of this green local actuation could have a huge impact on global energy demand.

Novel and innovative energy supply alternatives must be explored to remove or replace battery dependence and make feasible the deployment of these battery-free devices. Focusing on this field, a new trend in the research of energy sources for low-power applications has been growing rapidly during recent years. This approach consists in harvesting the available energy of the environment in order to supply sufficient power to electronic applications instead of using a battery or other technologies with short lifetime and finite amount of energy.

Power sources to harvest energy from the environment and technological solutions are quite abundant. The choice depends on the specific environment and application. This determines the sources of useful energy to be recovered and the available power levels.

The work presented is focused on the development of a low-power supply system based on the scavenged energy from different sources [53] present in the environment, in such a way that the system does not rely on only one harvesting source. Based on a low-voltage technology [54], an integrated solution is derived to recover energy at the microscale from different sources at the same time (vibration, light, and RF), as a proof of concept, recovering a total power higher than 1 mW.

The main objective is to eliminate the use of any standard battery and just work with the energy provided by the environment. This system is defined as the multiharvesting power chip (MHPC).

The developed power supply system, presented in this paper, will be the main part of the power management circuitry of a self-powered microsensor network which is still being designed.

The structure of this paper is as follows. Section III introduces the powering sources and their electrical models. The designed ICs that define the whole system are described in Section IV. Finally, Section V presents the experimental results of the power conditioning circuitry.

## II. CONCEPTION OF THE MULTIHARVESTING SYSTEM ARCHITECTURE

The MHPC consists in a simple IC capable of harvesting energy from different ambient sources and delivering this energy in usable electrical form. The proposed architecture is shown in Fig. 1.

The system is designed to collect energy from different ambient sources: solar (SC), mechanical vibration (using piezoelectric generators, PZT), and thermoelectrical energy (HEAT). Furthermore, it is also possible to recollect energy from an inductive power link (MI). All the energy obtained from these four sources is then transformed into electrical energy and stored in one or more storage devices (SDs). In the presented design developed to validate this approach, the MHPC works with three micropowering sources: light, vibration, and RF.

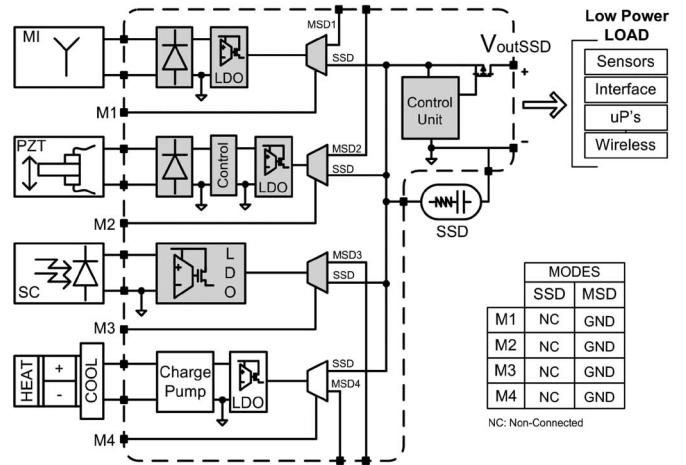


Fig. 1. MHPC diagram architecture and integrated modules in gray.

The idea consists of combining all the energy sources at the same time. In that way, energy from each source is added to that from other sources to obtain a total sum. Moreover, due to the nature of the conception, this multi-power-source scheme is robust against power failures. MHPC uses several independent power sources in one IC, and when one fails, the system is still producing energy owing to the other sources. Each power source uses its own energy conditioning circuit; in that way, all the sources can work together, in parallel and at the same time. Each module can be optimized in its operation, defining a peak-power tracker to optimize the operating condition and the efficiency of the system. For light powering, a nice solution is presented in [20]. In this paper, the authors present a novel approach to define the power tracking for solar-energy-harvesting circuits in a very simple way, depending on the illumination conditions, as a good approach for small low-power equipment. In the case of vibration, as presented in [84], the efficiency of the electromechanical conversion is quite high, ~80%. In our case, a particular power tracking for the RF and light modules has not been implemented. The roles of these kinds of solutions are well known individually, and for this proof of concept, the tradeoff between their inclusion in terms of power consumption and area is beyond the scope of the present work.

There are two operation modes when working with MHPC. The first one consists in using just a single SD (SSD) shared with all sources. The second mode consists in the use of each source separately from the others. In that mode, it is necessary to use multiple SDs (MSDs), one for each source. Using the second mode, it is possible to power more than one independent load at the same time, as described in [60], whereas using the first mode, it is possible to collect more energy in the SD but just power one common load.

Another important aspect consists of controlling the stored energy and how it is transferred to the load. Basically, the MHPC introduces a control module that manages this situation, as explained in more detail in Section IV. In the SSD operation mode, the control continuously senses the voltage at the storage element, and when there is enough voltage, the load is connected. From that point on, and if the voltage decreases to a minimum value also controlled by the control module, the load is disconnected. On the other hand, in MSD mode, it is possible

to integrate one individual control module for each source or just connect the source directly with the load.

Regarding the control module and the conditioning circuits, it is logical to assume that a low-power-consumption design is a necessity. Since an MHPC is a self-powered device and focused on low-voltage applications, low consumption is mandatory for all circuits in order to obtain good efficiency values. This implies that noncomplex power management circuits with low-power architectures and circuits have to be specifically designed.

A full-custom IC has been designed to validate the MHPC conception. The designed system is able to work with three different sources at the same time: solar energy (SC), mechanical vibration (PZT), and magnetic induction link (MI). The implemented integrated modules are colored in gray in Fig. 1. Thermoelectric source has also been included in the conception of the MHPC but, at this stage, is not integrated due to area limitations. For this type of powering source, small voltages are expected to be generated on chip. Then, in order to increase the voltage, a dc-dc converter is usually integrated, like in [50], particularly an autonomous efficient charge pump [51], with a linear regulator after the charge pump to regulate the dc voltage. These kinds of generators have been of considerable interest in recent years. They are based on a junction of two doped materials, namely, “n-type” and “p-type” semiconductors. These are connected by a metal conductor at the hot and at the cold side of the gradient. A temperature gradient across the thermoelectric material drives electron charge carriers from the hot to the cold junction and produces a voltage. TEGs are a good choice since they can be microfabricated with classical microfabrication techniques. In 1997, Stordeur and Stark designed the first micropower TEG that is able to produce  $20 \mu\text{W}$  with  $\Delta T = 20 \text{ K}$  [55]. Nowadays, some companies are selling products based on TEGs. For example, Seiko placed on sale a thermal wristwatch that uses ten thermoelectric modules to generate sufficient energy to run its mechanical clock [14]. There is also the Low Power Thermoelectric Generator by Thermo Life (Thermo Life Energy Corp., California), which is a TEG measuring  $0.5 \text{ cm}^2$  and  $1.6 \text{ mm}$  thick, that can supply energy to a biosensor when in contact with the skin. It is able to supply, with a  $5^\circ\text{C}$  gradient temperature,  $5 \mu\text{A}$  at  $3 \text{ V}$  [15].

Nonetheless, the MHPC validation has been completed without it.

### III. POWERING SOURCES

This section introduces the powering sources that have been used at this stage, which are the solar cells, piezoelectric generators, and the inductive link. Their electrical models and their compatibility with Spectre software, which has been used to validate the conception of the MHPC IC, are presented.

#### A. Solar Cells

A solar cell can be easily described as a large-area semiconductor diode (p-n junction) that is able to convert the energy of the incident light (energy of photons) into electrical current as a result of the photovoltaic effect [57].

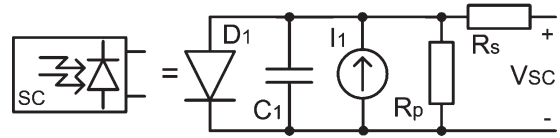


Fig. 2. Solar cell symbol and its equivalent circuit model.

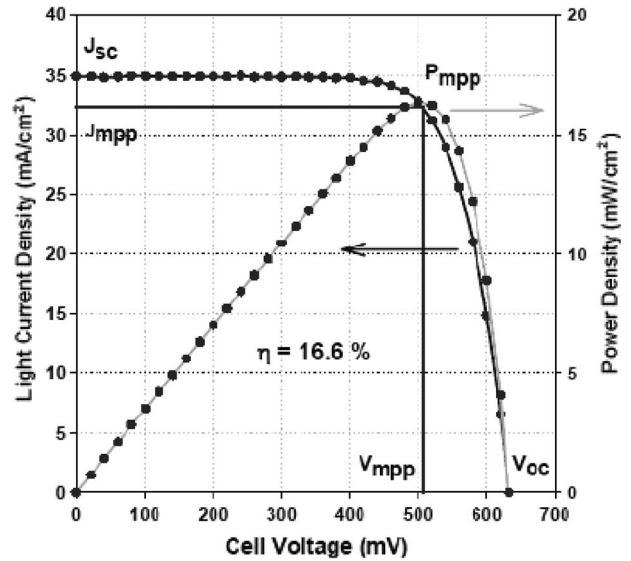


Fig. 3.  $I-V$  characteristic for a solar BIT from IXYS [59].

The basic equivalent circuit model of a solar cell is formed by a diode ( $D_1$ ) and a current source ( $I_1$ ) connected in parallel. The current source is proportional to the light radiation, whereas the diode represents the p-n junction.

Moreover, two resistors, one in series ( $R_S$ ) and the other in parallel ( $R_P$ ), could also be introduced in order to take into account the imperfections of the solar cell.  $R_S$  resistance is produced because a solar cell is not a perfect conductor, and  $R_P$  models its internal leakage current [58]. In an ideal cell, it is logical to assume  $R_S = 0$  and  $R_P = \infty$ . Sometimes, an extra capacitor ( $C_1$ ) is added to simulate the parasitic capacitance of the junction. Fig. 2 shows the symbol and the circuit model for solar cell.

A solar cell can also be described with its  $I-V$  waveform. Fig. 3 shows the  $I-V$  characteristics for a solar BIT from IXYS [56]. The generated current and voltage vary in function of the light conditions, although it is important to describe the following three quantities.

- 1) Open-circuit voltage ( $V_{oc}$ ): The voltage between the terminals when no current is flowing (infinite load resistance).
- 2) Short-circuit current ( $I_{sc}$ ): The current when there is a short circuit in the terminals (zero load resistance).
- 3) Maximal power point (MPP): Point of the solar cell when it produced the maximum amount of power.

The IXYS XOB17 solar cell is used in that work as a solar generator. It is a high-efficiency indoor/outdoor monocrystal silicon solar cell mounted in a Surface Mount Device (SMD) mechanical package ( $22 \text{ mm} \times 7 \text{ mm} \times 1.6 \text{ mm}$ ) consisting of three XOD17 solar cell units. It presents an efficiency of typically 17%, and the characteristics are listed in Table II.

TABLE II  
IXYS XOB17 ELECTRICAL CHARACTERISTICS

Symbol	Parameter	Value	Units
$V_{OC}$	open circuit voltage	1.89	V
$I_{SC}$	short circuit current	12.6	mA
$V_{MPP}$	voltage @ MPP	1.53	V
$I_{MPP}$	current @ MPP	11.7	mA

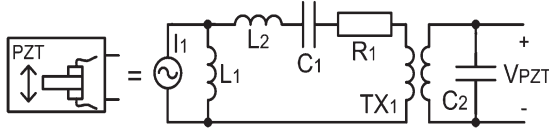


Fig. 4. PZT symbol and its electrical circuit model.

TABLE III  
QP20W ELECTRICAL CHARACTERISTICS

Acceleration	Voltage	Current	$R_{LOAD}$
$7m/s^2 @ 82 \text{ Hz}$	1.2 V	$75\mu A$	10k $\Omega$

### B. Piezoelectric Generators

The piezoelectric generator used is based on the Quick Pack QP20W (Midé Technology Corporation, Medford, MA). The Quick Pack QP20W [35] is a composite beam made of two piezoelectric layers working as a bimorph body, with an intermediate layer made of polyamide.

This composite beam is then located with one end clamped to a vibrating body and the other end remaining free. The vibrations forced at the clamped end are propagated along the cantilever beam. This wave generates an induced strain in the membrane, which, at the same time, produces an electrical charge. The piezoelectric membranes generate an unregulated ac voltage. Thus, they cannot be connected directly with the load because it generally requires dc voltage.

In order to be able to recover this energy, a lumped electrical model that is compatible with Spectre software has been developed. The model is based on the modal analysis of piezoelectric Euler–Bernoulli beam equations [60], [61]. Solving the beam equation for the first resonance mode, and considering the equivalences between the equations defining a mechanical system and the equations defining an electrical circuit, an electromechanical equivalent circuit is proposed. In the experimental setup for model identification and validation, the transducer is mounted and clamped over an electromagnetic vibration shaker ET-132 (Labworks Inc., Costa Mesa, CA). The shaker is driven with a specific linear power amplifier Pa-119-2M (Labworks Inc.), with the command signals coming from a function generator. For the displacement measurements, a triangulation laser LC2440 from Keyence is used.

Each of the electrical components, appearing in the equivalent circuit (Fig. 4), has been defined by means of the beam geometrical and material parameters.

Table III summarizes the features for this model, just in the case of an output voltage of 1.2 V. The maximum voltage available is 2.5 V, requested by the technological limitations.

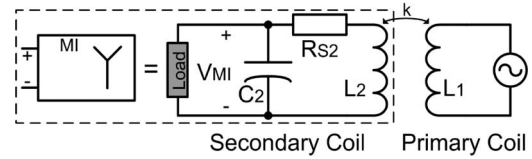


Fig. 5. Inductive power link symbol and its electrical circuit model.

### C. Inductive Power Link Model

Wireless power link, also known as wireless power transmission, is the way to transfer energy without wires; thus, it is the manner to transfer electricity through an electromagnetic field [62]–[65]. There are several types of wireless power transmission, namely, radiative [66], conductive [67], capacitive [68], and inductive [69], but this work is only focused on inductive low-power transmission.

An inductive link is mainly composed by two coupled coils, as shown in Fig. 5. One works as a primary or transmitting coil ( $L_1$ ), where the power is injected and emitted, and the other works as a secondary or receiving coil ( $L_2$ ), where the total or a partial part of the emitted power is received. Examples of contactless energy transfer systems for high-power applications are shown in [70] and [71].

The transmission principle consists of injecting an ac current through the primary coil generating an ac magnetic field. The secondary coil then recovers this magnetic field or just a portion of it, and an electromotive force is generated, which is used as a voltage source by the load connected to the receiving coil. This transmission method is also called a transcutaneous energy transfer system [69] when the links are used in human implantable devices [72].

Moreover, inductive transmission presents some advantages if one of the possible applications regards the human body and implantable electronics. It is the best solution to develop a near-field link in the range of 1–15 MHz [68] to transmit energy through the human skin. This range of frequencies assures minimal losses due to the power absorption of the skin [73], and since the coils are coupled and tuned to work specifically in one frequency, the electrical drifts are minimal [73] to the surrounding biological area. In our proof of concept, this is the option that has been adopted to combine vibration and indoor light energy with electromagnetic energy recovery.

The secondary coil usually works in resonance to increase the link efficiency and to be selective with the used frequency. The resonance is achieved by adding a capacitor in series or parallel to the secondary coil. If the link uses a parallel-resonance secondary coil, it works as an output voltage source, whereas the series one operates as a current source.

The designed coils work in parallel resonance by adding an extra capacitor ( $C_2$ ), as shown in Fig. 5. Parallel resonance presents better performances for high loads than the series one. Furthermore, the parasitic capacitance of the secondary coil ( $L_2$ ) is absorbed by the tuning capacitor. The resonant frequency of the  $L$ – $C$  tank, no load connected, is defined by

$$w_2^{Ideal} = \frac{1}{\sqrt{L_2 C_2}}. \quad (1)$$

This equation is used to calculate the tuning capacitor for a specific given frequency. It is important to notice that the resonance frequency is modified when the load is connected to the secondary coil, as it is described in (2). This derives that, for low load values, high current, the resonant frequency is widely modified, hence low efficiencies. Therefore, the parallel-resonance secondary circuit is suitable to be used with large loads [76], [77]

$$w_2^{\text{Real}} = \frac{1}{\sqrt{L_2 C_2}} - \frac{1}{\sqrt{R_{\text{Load}}^2 C_2^2}}. \quad (2)$$

The coupling factor  $k$  between coils is another important parameter to take into account. The power link efficiency is mainly dominated by  $k$ . Horizontal and vertical misalignments, as well as large distances between both coils, affect the coupling factor, reducing the efficiency of the link. The total link efficiency expression for secondary parallel resonance is given by

$$\eta = \frac{k^2 Q_1 Q_2}{\left(1 + \frac{Q_1}{w C_2 R_{\text{Load}}} + k^2 Q_1 Q_2\right) (w C_2 R_{\text{Load}} + Q_1)}$$

$$Q_1 = \frac{w L_1}{R_{S1}}$$

$$Q_2 = \frac{w L_2}{R_{S2}} \quad (3)$$

where  $Q_1$  and  $Q_2$  are the quality factors of the primary and secondary coils, respectively. The efficiency is independent regardless if the primary coil is tuned or not. The maximal efficiency is obtained for

$$R_{\text{Load}}^{\eta_{\text{MAX}}} = \frac{Q_2}{(1 + \sqrt{1 + k^2 Q_1 Q_2}) w C_2}. \quad (4)$$

Then, the maximal link efficiency is just substituting (4) into (3)

$$w_2^{\text{Ideal}} = \frac{1}{\sqrt{L_2 C_2}} \quad \eta_{\text{MAX}} = \frac{k^2 Q_1 Q_2}{(1 + \sqrt{1 + k^2 Q_1 Q_2})^2}. \quad (5)$$

A rectangular coil has been designed on a printed circuit board in order to work as a secondary coil for harvesting applications. It is tuned to the RFID frequency of 13.56 MHz (ISM band). Typically, for an input power of 200 mW for the primary and an efficiency of 50%, an on-chip current of a few milliamperes can be achieved. A TRF7960 [78] from Texas Instruments is used as a primary source. Table IV summarizes its main characteristics.

An accurate description and a calculation methodology to develop an inductive link for harvesting and implantable devices can be found in [71]–[74]. In the same way, studies in [75]–[77] explain several options to design different types of coils.

Recently, an interesting work has been published in the field of harvesting, as one step further RF coupling as a way to recover energy, particularly for biomedical applications [79]. This option is based on ultrasonic powering instead of RF powering, generating up to 1 V and a power capability of 21.4 nW.

TABLE IV  
RECTANGULAR COIL CHARACTERISTICS

Symbol	Parameter	Value	Units
$L_2$	secondary coil	220	nH
$C_2$	parallel capacitor	620	pF
$R_{S2}$	secondary series resistance	310	m $\Omega$
$f$	Resonance frequency	13.56	MHz
$N$	number of turns	3	-
CW	Conductor width	1	mm
SUB	type of substrate	FR4	-
L x W	dimensions	30 x 15	mm

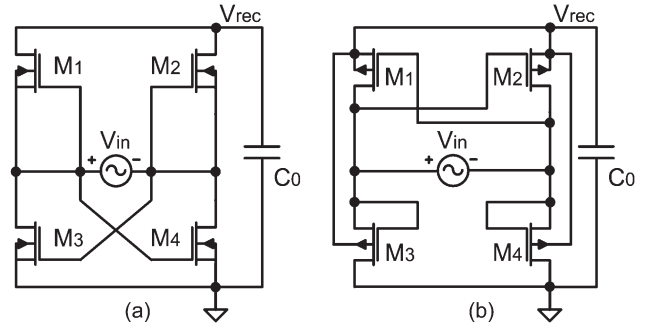


Fig. 6. (a) NMOS and (b) PMOS full-wave rectifiers.

#### IV. MULTIHARVESTING IC ELECTRONICS

The MHPC circuitry combines three main circuits: an integrated rectifier needed to rectify the ac signal coming from the piezoelectric source, or from the electromagnetic source; a low-voltage low-power regulator core, based on a bandgap (BG) circuit used to define a reference voltage, and a low-dropout regulator; and, finally, a control unit (Fig. 1).

##### A. Rectifier Circuits

Since the PZT generator supplies an ac voltage, a rectification stage is needed. Two different rectifiers [62], [80] based on the diode bridge configuration are presented, based on the use of NMOS or PMOS transistors.

A bridge rectifier based on NMOS transistors is shown in Fig. 6(a). The voltage is rectified as follows: When the input voltage polarity is positive, the current flows through transistors  $M_1$  and  $M_4$ , and transistors  $M_2$  and  $M_3$  are switched off. When the polarity is reversed, where  $V_{in-}$  is higher than  $V_{in+}$ , the current flows through transistors  $M_2$  and  $M_3$ , while  $M_1$  and  $M_4$  are shut off.

Fig. 6(b) shows the architecture of the PMOS bridge rectifier. When voltage  $V_{in+}$  is higher than  $V_{in-}$ , transistors  $M_2$  and  $M_3$  are activated, whereas  $M_1$  and  $M_4$  are shut off. On the other hand, when voltage  $V_{in-}$  is higher than  $V_{in+}$ , transistors  $M_2$  and  $M_3$  are deactivated, and  $M_1$  and  $M_4$  are turned on.

When working with MOSFET rectifiers, a tradeoff in terms of efficiency and area has to be analyzed. A low drop voltage across the transistors implies high channel width and low-frequency operation; on the other hand, small channel width represents a higher drop voltage and high operation frequencies. Fig. 7 shows the rectified voltage ( $V_{\text{rec}}$ ) and the operation

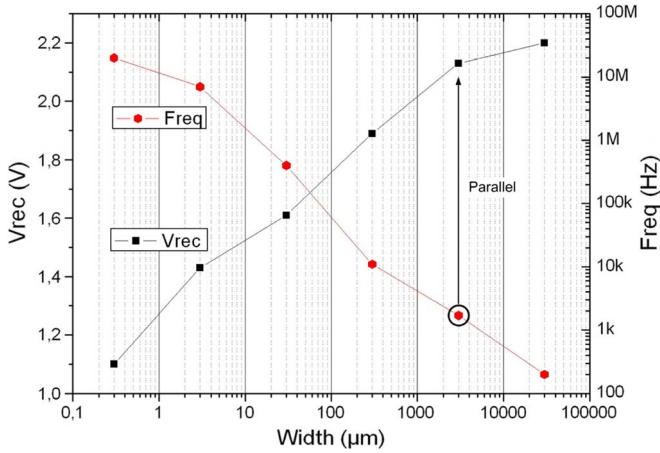


Fig. 7. Rectified voltage ( $V_{rec}$ ) and operation frequency in function of transistor width for the NMOS full-wave rectifier of Fig. 6(a) ( $L = 1 \mu\text{m}$  and  $V_{in} = 5 \text{ Vpp}$  at 500 Hz).

frequency  $Freq$  for the NMOS rectifier in Fig. 6(a), as a function of a single NMOS transistor width. A sinusoidal signal of 5 Vpp at 500 Hz is used as input.

When the input voltage value is low and at low frequencies, like when working with PZT, it is a good option to select high-width transistors with low drop voltages. On the other hand, when working at higher frequencies, like in inductive powering, small widths are a good choice in order to increase the switching frequency. There is an optimal operation point in the intersection of both waveforms, but if the desired working frequency and the expected rectified voltage are higher than those obtained at the optimal point, some extra considerations have to be made.

Several transistors in parallel can be connected to improve the performance of the rectifier in terms of voltage drop and frequency. This configuration divides the current into all transistors, reducing the drop voltage ( $V_{ds}$ ) of each parallel NMOS. Hence, it is possible to improve the working frequency because the size of all individual transistors is smaller than just one big transistor.

Taking into account the previous considerations, an integrated NMOS rectifier [Fig. 6(a)] formed by four transistors— $M_1$ ,  $M_2$ ,  $M_3$ , and  $M_4$ —of 3000- $\mu\text{m}$  width is implemented. This size involves a voltage-drop range of 0.2–0.6 V depending on the technological drifts. To solve the problem of low working frequency due to size, the black circle in Fig. 7, a parallel structure of 300 transistors of 10  $\mu\text{m}$  is used to form each transistor. Hence, a new working frequency range of 3–15 MHz is achieved depending on the technological drifts.

An efficiency range between 55% and 85% is achieved depending on the load and frequency conditions. In the case of high load, the efficiency decreases due to the voltage drop across the transistors. On the other hand, a better efficiency is obtained in the case of low current loads: The lower the current flowing through the rectifier, the lower the drop voltage through it, and thus, the higher the efficiency.

The operating frequency also affects the efficiency of the rectifier. For higher frequencies, the transistors' leakage increases, producing more losses, and therefore, the efficiency decreases.

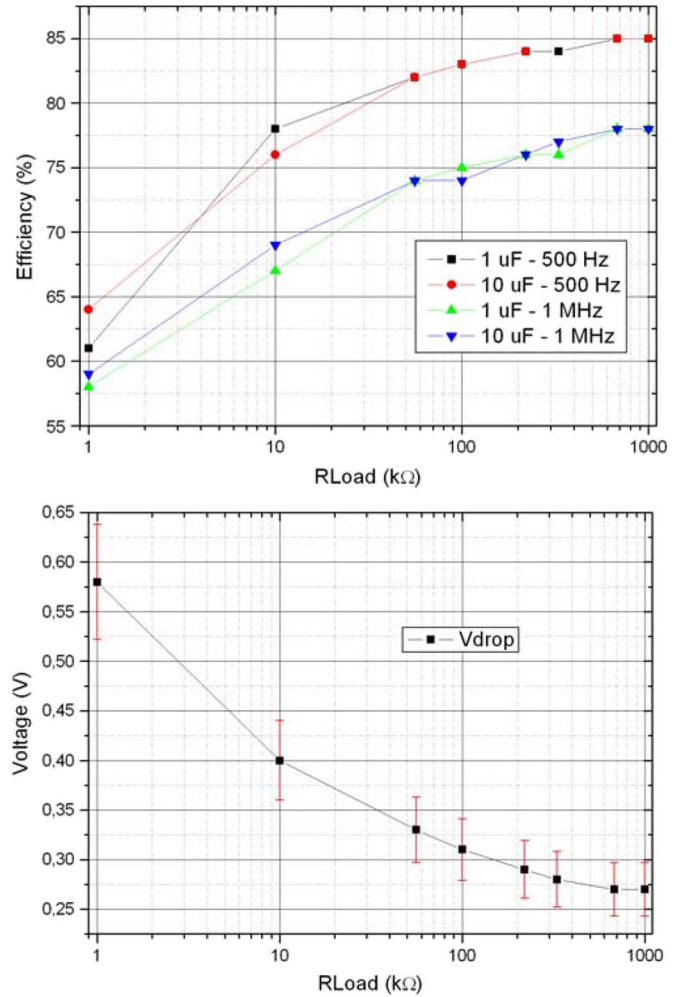


Fig. 8. NMOS rectifier efficiency and voltage drop for several load conditions.

Fig. 8 shows the efficiency of the rectifier versus several load conditions for different frequencies and filter capacitances ( $C_0$ ) and the voltage drop across the rectifier in function of load conditions. A tradeoff in terms of area, load current, leakage, and voltage drop has to be reached to fit the correct rectifier in each application. In addition, a minimum input voltage higher than the threshold voltage of the transistors is necessary to activate them properly and rectify the incoming signal.

Table V summarizes the main features of the rectifier, and Fig. 9 shows the minimum input voltage that is able to be properly rectified by the NMOS ac/dc converter. The PMOS rectifier presents a simulated efficiency of 72% under the same conditions as the NMOS. In spite of its better efficiency, the NMOS rectifier is integrated due to its reduced dimensions. The PMOS rectifier is ten times higher than the NMOS.

B. Regulator Core

This circuitry is based on two modules that are used in the different modules, a BG circuit and an LDO regulator.

The proposed BG circuit is based on a full MOSFET BG architecture [81], [82] in order to avoid the use of bipolar transistors [83], [84], because these transistors are not available

TABLE V  
 NMOS FULL-WAVE RECTIFIER CHARACTERISTICS

Symbol	Parameter	Min	Max	Units
$V_{IN}$	nominal input voltage	0.3	2.5	Vp
$V_{drop}$	drop voltage	0.2	0.67	V
$I_{out}$	output current	-	20m	A
Freq	working frequency	-	16M	Hz
$\eta$	efficiency	52	85	%
$I_{leakage}$	leakage current	-	1.4m	A
W	width of each transistor	3000 $\mu$		m
L	length of each transistor	0.28 $\mu$		m

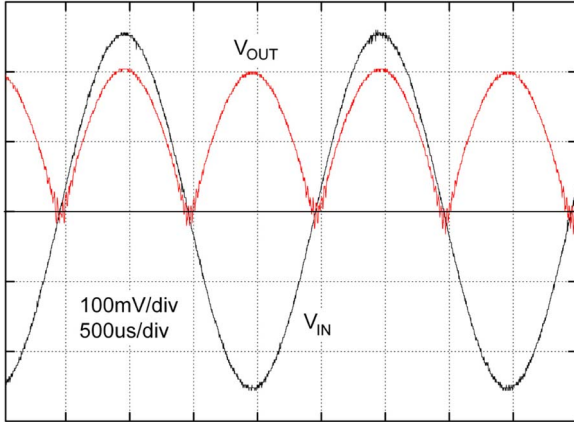


Fig. 9. NMOS rectifier minimum input voltage.

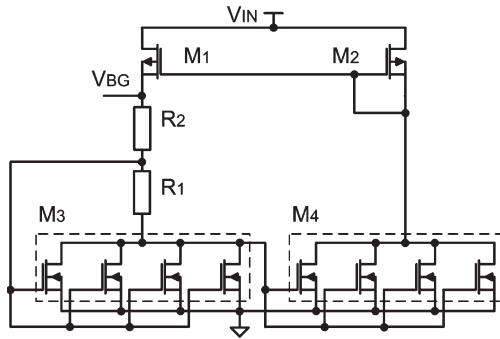


Fig. 10. Schematic of the BG circuit.

in the technology used. This circuitry has been presented in [85]. The full MOSFET BG architecture is shown in Fig. 10.

Several simulations have been carried out, obtaining a nominal value of the reference voltage of 530 mV for this design. The power dissipation is 10  $\mu$ W at 1.4 V, which represents low power consumption.

Fig. 11 shows the experimental BG voltage against temperature at  $V_{cc} = 1.2$  V. The results show the experimental values for four application-specified ICs (ASICs): IC1, IC2, IC2, and IC4. In addition, in Fig. 11, the experimental voltages are compared with the simulated BG voltages for different statistical models supported for the selected technology and the Spectre simulator: SSA (slow case), which means slow mobility for the carriers; TTY (typical case), which means an average mobility for the carriers; and, finally, the FFA model (fast case), which means the highest mobility for the carriers.

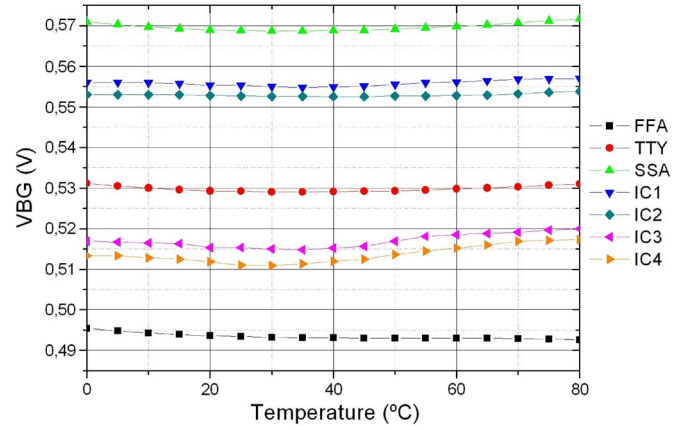


Fig. 11. BG voltage versus temperature for four different ICs.

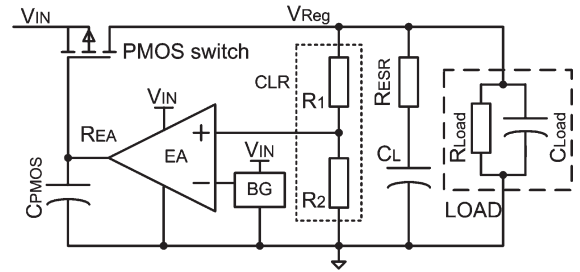


Fig. 12. LDO regulator architecture.

The implemented LDO regulator architecture is shown in Fig. 12. It is formed by one switch, one error amplifier (EA), a voltage BG reference circuit, and the closed-loop resistors (CLR)s used to regulate the output voltage. It is designed to generate a nominal regulated voltage ( $V_{Reg}$ ) of 1.2 V. The regulated voltage is defined by the CLR as

$$V_{Reg} = V_{BG} \left( 1 + \frac{R_1}{R_2} \right). \quad (6)$$

The selected switch is a PMOS transistor. An NMOS switch implies positive voltages to drive its gate, and the signal generation becomes difficult when working at low voltages. The low-voltage control and low dropout voltages of the PMOS transistor are perfect for this application.

The design of the LDO has to follow these two main constraints: the lowest possible consumption and the smallest possible area. The consumption depends on the power dissipation of the internal circuits such as the current source, the voltage reference circuit, and EA. In terms of area, it is logical to assume that the smallest possible area is the most desirable solution to integrate the LDO in a system like MHPC.

Taking into account the stability issues and the power and area constraints, the LDO has been designed in accordance with the idea of a compensation by an external dominant pole [85]–[88]. This means that the LDO will use an off-chip capacitor ( $C_L$ ) to guarantee stability for all load conditions.

To analyze the stability, it is important to evaluate the position of the poles and zeros of the LDO. The generic LDO has three poles in its frequency loop transfer. The first pole (P1) is basically defined by the output resistance of the switch, the load resistance, and the series resistance ( $R_{ESR}$ ) of the output

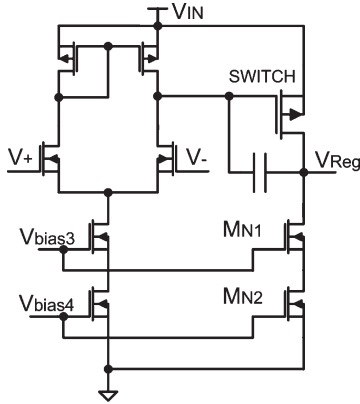


Fig. 13. EA and PMOS switch.

capacitor  $C_L$  (Fig. 12). The second pole (P2) is related to the gate capacitance of the PMOS switch and the output resistance of the EA ( $R_{EA}$ ). The first pole, P1, is the dominant one. This pole has the characteristic that it varies depending on the load current level in the low frequency range. Finally, the ESR resistance and the equivalent load capacitance define the third pole, P3.

Typically, the  $R_{EA}$  resistance is high, and the  $C_{PMOS}$  is small. Hence, P2 is also placed at medium/high frequencies, which causes the response of the LDO to be slow. However, in this system, there is also the presence of a zero, which is typically related to the  $R_{ESR}$  resistance. In that way, the zero is located at higher frequencies than P1 and, at the same time, at lower frequencies than the unity gain frequency (UGF), pushing the LDO into a stable situation.

In summary, there are a dominant pole (P1) working at low frequencies and another pole (P3) working at frequencies higher than UGF. Furthermore, P2 is working at medium/high frequencies but lower than UGF, which makes stability difficult. For that reason, the placement of the zero (Z0) at lower frequencies than UGF helps the stability of the LDO.

The stability of the LDO by a dominant pole is effective, but a high value of  $C_{LOAD}$  is required. It is not difficult to obtain a high-value capacitor when working with harvesting applications because the storage element always presents a high capacitance value. The speed of the LDO is typically several milliseconds (around 25 ms).

The EA is based on a two-stage amplifier as is shown in Fig. 13. Transistors  $M_{N1}$  and  $M_{N2}$  are used to define the ground current in the case of no-load conditions. Table VI summarizes the most important features of the implemented LDO.

Fig. 14 shows the experimental case of a regulated voltage ( $V_{Reg}$ ) of 1.196 V obtained from an unregulated dc voltage of 1.5 V provided by the solar cells at indoor illumination conditions of 1000 lx (fluorescent tubes). A 4.7-nF external capacitor ( $C_L$ ) works as an SD and compensates the LDO.

### C. Control Unit

The control unit has been designed and is based on a previous solution presented in [85]. The architecture of the unit is shown in Fig. 15. The dc voltage is used to charge the voltage at the

TABLE VI  
LDO ELECTRICAL CHARACTERISTICS

Symbol	Parameter	Min	Max	Units
$V_{IN}$	input voltage	1.3	2.5	V
$V_{Reg}$	regulated output voltage	1.189	1.22	V
$I_{Reg}$	output current	20 $\mu$	10m	A
$I_{CC}$	current consumption	23 $\mu$	27 $\mu$	A
$P_{CC}$	power consumption	29 $\mu$	67 $\mu$	W
$\Delta_{Load}$	load regulation*	13m	34m	V
$\Delta_{Line}$	line regulation**	7m	18m	V
$\Delta_{DC}$	DC gain	63	72	dB
$P_M$	phase margin	58	65	$^\circ$
PSSR	supply rejection ratio	28.7	39.4	dB

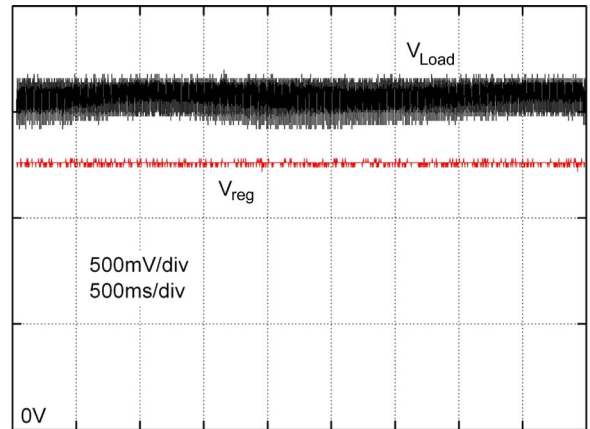


Fig. 14. Solar cell + LDO experimental result.

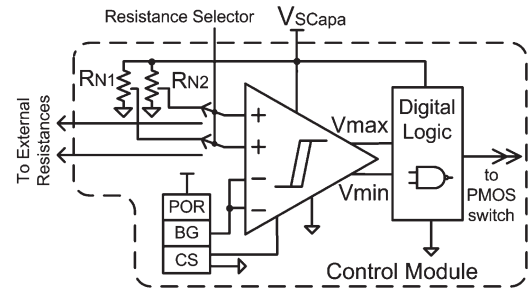


Fig. 15. Complex control module architecture.

SSD element, as shown in Fig. 1. This voltage is monitored continuously by the control module and compared with two trigger values ( $V_{max}$  and  $V_{min}$ ) in order to control the PMOS switch.

When the dc voltage at SSD element reaches the maximum value ( $V_{max}$ ), the control module switches on the PMOS transistor, and the energy stored in the capacitor or battery is transferred to the load. At that point, SSD starts to decrease (discharging phase) to a minimum voltage value ( $V_{min}$ ). When the control module senses the minimum threshold value, the PMOS is automatically deactivated, and the voltage transference from the capacitor to the load stops. Immediately, the voltage at the SSD increases again up to  $V_{max}$ , defining the recharge phase. It must be stated that the load must work between  $V_{max}$  and  $V_{min}$  voltages. The first time the battery is charged to  $V_{max}$  is defined as the start-up phase.

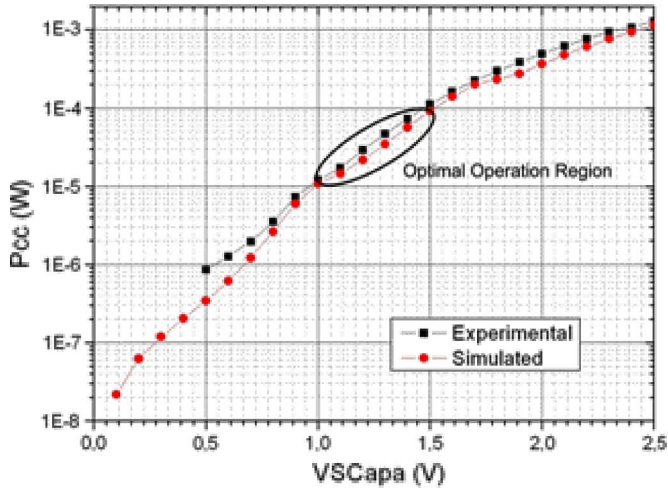


Fig. 16. Complex module power consumption.

The  $V_{max}$  value is defined by the regulated dc voltage defined by the LDO regulators. The  $V_{min}$  is the dc nonregulated minimum voltage acceptable for the loads to work.

The time involved in the start-up and recharge phase varies in function of the power available by the generator and the value of the capacitor. The discharge phase time depends on the load power consumption. The energy is transferred to the load in pulses, defining a burst operation mode: The load is only connected if there is enough energy at the capacitor. It is possible to move from burst mode toward continuous mode if the load consumption is lower than the generated power. In that way, the load capacitor does not reach the minimum threshold voltage, and a long-operation discharge phase is defined.

The system is formed by two low-power comparators (Fig. 15), which continuously sense the voltage at the storage capacitor SSD and compare it with a reference voltage supplied by a BG reference circuit. Two resistive networks,  $R_{N1}$  and  $R_{N2}$ , are used to adapt the voltage level of SSD to the range defined by the BG. One comparator is set to detect when the voltage reaches  $V_{max}$  and the other to sense  $V_{min}$ . The signals generated by the comparators are used by a logic circuitry to generate the control signal for the PMOS switch and to define the charge and discharge phases of the system. The comparators, the digital logic, and the rest of the elements of the control unit are powered by the voltage at the storage element SSD.

The complex control also incorporates a power on reset (POR). This circuit is used to reduce the power consumption of the module during the start-up phase. At the beginning, when the voltage grows from zero to  $V_{max}$  for the first time, only the POR and the BG circuit are working. When the voltage at the storage capacitance is around 0.8 V, the POR circuit activates the rest of the electronics, increasing the power consumption of the module. In that way, the system is only connected when a minimum amount of voltage is available at the SD. The power consumption of the module is shown in Fig. 16, where it is compared with the typical simulated values. In that case, the simulated and experimental results are, in fact, similar.

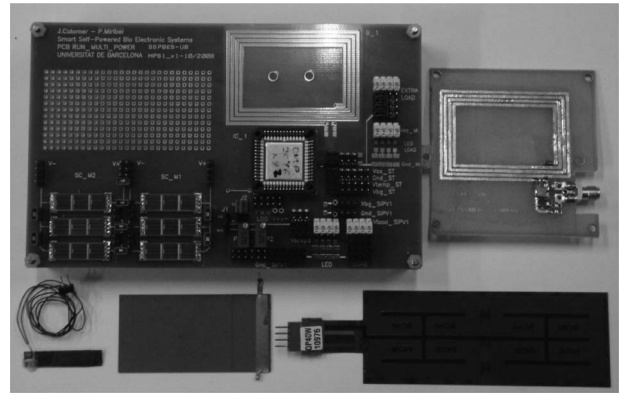


Fig. 17. MHPC demo board.

### V. EXPERIMENTAL RESULTS

The IC has been designed in a 0.13- $\mu\text{m}$  technology which is a low-voltage technology, up to 3.3 V. This IC works in an environment where light, vibration, and RF sources are used to recover energy. External off-chip Zener diodes [51] are used to protect the circuitry. It must be stated that, for the maximum conditions of operation of the three microenergy sources, the ASIC always works in a safe operating region.

From Fig. 1, signals  $M_1-M_4$  control the connection of each power source. A control module is included in order to work in SSD mode.

The IC has been tested with the demo board shown in Fig. 17. Six solar cells, XOB17, from IXYS [59] are used to harvest solar energy. Each one of them could be connected with the others using a serial or parallel connection. Several piezoelectric transducers are used to handle the mechanical vibration. The main tests were done with two piezos from Mide. Tech. (QP20W and QP40W) [35] and the electromagnetic vibration shaker ET-132 (Labworks Inc.). The presented results were obtained with two stacked QP20W in parallel working at 7  $\text{m/s}^2$  at 80 Hz.

Regarding magnetic induction link, a planar rectangular antenna (inductor) of 30 mm  $\times$  15 mm is added to the board in order to operate as a secondary antenna. It has three turns, a conductor width of 1 mm, and an inductance of 220 nH. It is tuned to work in the RFID range of 13.56 MHz. A Texas Instruments TRF7960 is used as the primary source.

Fig. 18 shows the working principle of the MHPC working in SSD mode: just one SD shared with all sources. This depicts the current used to charge the SD and how it increases or decreases depending on the number of activated sources. The voltage at the SD is regulated at 1.2 V. Maximum current is flowing to the SD (5 mA) when the three sources, namely, solar (SC), piezoelectric (PZT), and inductive link (MI), are working together.

This particular test is done with the QP40W piezoelectric working at 1  $\text{m/s}^2$  at 80 Hz, two IXYS solar cells at indoor light conditions of 1500 lx, and the RF link generator TRF7960 emitting at full power (200 mW), with a distance between the base station and the antenna receiver of 25 mm.

Full system is able to recover, with the three powering sources working at the same time, a total power of 6.2 mW.

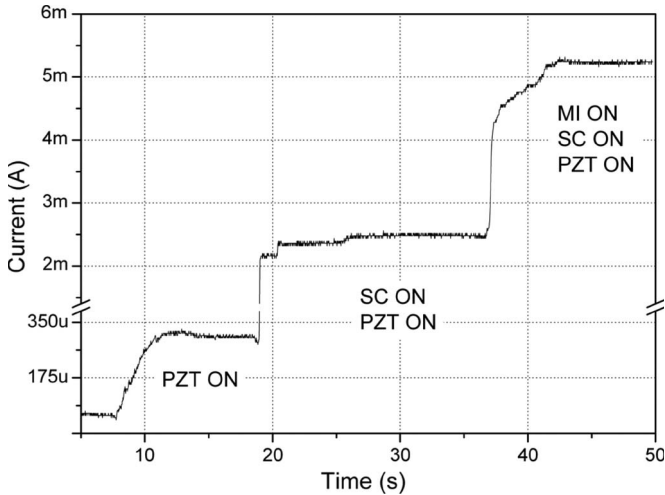


Fig. 18. MHPC powering source addition.

The power harvested using the light in the office illumination conditions alone is 2.76 mW. When operating with just the RF module, based on inductive coupling, the recovered power is 4.5 mW. Finally, the vibration harvesting working alone is able to recover up to 360  $\mu$ W. Ideally, the addition of the three powering sources working in the SSD mode would be 7.8 mW. It must be stated that the quiescent power consumption of each LDO is around 30  $\mu$ W and that the control module has a power consumption of around 70  $\mu$ W. Then, when the three sources are combined, the ASIC has an additional power consumption of 60  $\mu$ W. The difference of 1.6 mW between the theoretical addition of the harvested power and the real amount of power that is recovered is due to the variation of the effective load conditions for the light and RF modules, mainly because the PZT module is working practically in the best electromechanical conversion conditions [85].

For the light and RF modules, some power tracking can be designed. Regarding the RF module, a solution to harvest energy following the peak power point of an antenna and the integrated rectifier source is presented in [90]. For the light module, a solution based on the study in [20] can be designed. However, as stated earlier, at this stage of the prototype, our objective is to validate the conception of the MHCP circuitry.

The implementation of some tracking solutions for the peak power point for the RF and light modules involves a study of the power consumption of such solution, and their cost in silicon area, compared with the improvement that could be achieved. Simple solutions should be adopted in order to avoid complex control algorithms and power consumption.

## VI. CONCLUSION

This paper has presented a full-custom MHPC for a self-powered system based on the addition of different harvesting power sources: vibration energy scavenging based on a low-cost piezoelectric commercial generator, solar energy, and electromagnetic induction, in order to validate the concept of the IC.

The whole architecture has been designed using a low-power low-voltage commercial technology. The design of the system is based on the use of a validated model of the piezoelectric

TABLE VII  
MHPC INPUT PIN MAXIMUM ELECTRICAL FEATURES

Symbol	Parameter	Min	Max	Units
$V_{IN\ PZT}$ $I_{IN\ PZT}$	input voltage Piezo input current Piezo	+/- 1 -	+/- 2.5 5	Vac mA
$V_{IN\ SC}$ $I_{IN\ SC}$	input voltage Solar Cell input current Solar Cell	1.3 -	2.5 10	Vdc mA
$V_{IN\ MI}$ $I_{IN\ MI}$	input voltage Induction input current Induction frequency of operation (up to 25 MHz)	+/- 1.3	+/- 2.5 10	Vac mA

micropower generator, inductive link, and solar cells. The architecture of the proposed MHPC is presented, and each circuit block is also described in detail.

Experimental results confirm the correct performance of the adopted architecture integrated in a commercial technology, defining a multimode energy scavenging prototype, which combines the capture of energy from vibrations at low frequencies, indoor ambient light, and inductive coupling.

As a point-of-view system, the addition of three microharvesting sources has been validated. The total harvested power, at the indicated nominal conditions, is greater than 5 mW. This device, in the suitable ambient conditions, would be able to power enough energy for a typical sensor node. The power is strongly dependent on the complexity of the sensor, in terms of the measurements to be done and the data rate to be transmitted. Some examples of the power level that can be assured by such devices are described in [91] and [92]. In [91], the temperature is measured and transmitted every 5 s, with a power consumption of 10  $\mu$ W. In [92], a pulse oximeter sensor is powered by 90  $\mu$ W.

In summary, the power level of 200  $\mu$ W is a good value that represents the average power level needed by a sensor node to measure and transmit data rates of 200 kb/s [93].

An interesting feature would be the use of MEMS technologies with the ASIC production. Micromachining will allow the production of cheaper devices by combining these different types of powering sources with specific microgenerators for specific environments and applications.

At this stage of the research, no peak power operating for each module has been implemented. Future work is oriented to analyze the possibility of including them in order to increase the whole efficiency but analyzing the tradeoff between the area and power consumption of these solutions, which necessarily requires very low power consumption and small area, to avoid increasing the cost of the system.

Table VII shows the main features of the MHPC in terms of its electrical characteristics. These are the minimum and maximum voltages and currents available for this prototype for the three types of powering sources considered: vibration based on piezoelectric generators (PZT), light based on indoor solar cells (SC), and, finally, electromagnetic induction (RF). The operating conditions of the microharvester, imposed by the application and environment of use, must fit these ranges. Table VIII shows the electrical features of the prototype for the MSD mode, which is that every powering source has its own

TABLE VIII  
MHPC OUTPUT PIN MAXIMUM ELECTRICAL FEATURES IN  
FUNCTION OF THE MODE OF OPERATION

	Symbol	Parameter	Min	Max	Units
MSD MODE	V <sub>OUT</sub> PZT	output voltage	1	2.5	Vdc
	I <sub>OUT</sub> PZT	output voltage	-	10	mA
	V <sub>OUT</sub> SC	output voltage	-	1.2	Vdc
	I <sub>OUT</sub> SC	output voltage	-	10	mA
	V <sub>OUT</sub> MI	output voltage	-	1.2	Vdc
	I <sub>OUT</sub> MI	output voltage	-	10	mA
SSD MODE	V <sub>OUT</sub>	output voltage	1	1.2	V
	I <sub>OUT</sub>	output voltage	-	20	mA

SD, or the SSD mode, where the three powering channels share the same SD, which can be a supercapacitor. In our case, as a test approach for Fig. 18, a capacitor of 47 μF was used.

REFERENCES

[1] S. Alepuz, S. Busquets-Monge, J. Bordonau, J. Gago, D. Gonzalez, and J. Balcells, "Interfacing renewable energy sources to the utility grid using a three-level inverter," *IEEE Trans. Ind. Electron.*, vol. 53, no. 5, pp. 1504–1511, Oct. 2006.

[2] J. M. Carrasco, L. G. Franquelo, J. T. Bialasiewicz, E. Galvan, R. C. PortilloGuisado, M. A. M. Prats, J. I. Leon, and N. Moreno-Alfonso, "Power-electronic systems for the grid integration of renewable energy sources: A survey," *IEEE Trans. Ind. Electron.*, vol. 53, no. 4, pp. 1002–1016, Jun. 2006.

[3] J. Schonberger, R. Duke, and S. D. Round, "DC-bus signaling: A distributed control strategy for a hybrid renewable nanogrid," *IEEE Trans. Ind. Electron.*, vol. 53, no. 5, pp. 1453–1460, Oct. 2006.

[4] L. Collins, "Harvest for the world," *IEE Power Engineer*, vol. 20, no. 1, pp. 34–37, Feb./Mar. 2006.

[5] J. A. Paradiso and T. Starner, "Energy scavenging for mobile and wireless electronics," *IEEE Pervasive Comput.*, vol. 4, no. 1, pp. 18–27, Jan.–Mar. 2005.

[6] E. M. Yeatman, "Energy scavenging for wireless sensor nodes," in *Proc. 2nd Int. Workshop Adv. Sens. Interface*, Jun. 2007, pp. 1–4.

[7] S. Roundy, D. Steingart, L. Frechette, P. Wright, and J. Rabaey, "Power sources for wireless sensors networks," in *Proc. 1st Eur. Workshop Wireless Sens. Netw.*, Jan. 2004, pp. 1–17.

[8] D. Niyato, E. Hossain, M. M. Rashid, and V. K. Bhargava, "Wireless sensor networks with energy harvesting technologies: A game-theoretic approach to optimal energy management," *IEEE Wireless Commun.*, vol. 14, no. 4, pp. 90–96, Aug. 2007.

[9] L. Garbuio, M. Lallart, D. Guyomar, C. Richard, and D. Audigier, "Mechanical energy harvester with ultralow threshold rectification based on SSHI nonlinear technique," *IEEE Trans. Ind. Electron.*, vol. 56, no. 4, pp. 1048–1056, Apr. 2009.

[10] T. T. Le, J. Han, A. von Jouanne, K. Mayaram, and T. S. Fiez, "Piezoelectric micro-power generation interface circuits," *IEEE J. Solid-State Circuits*, vol. 41, no. 6, pp. 1411–1420, Jun. 2006.

[11] M. E. Kiziroglou, C. He, and E. M. Yeatman, "Rolling rod electrostatic microgenerator," *IEEE Trans. Ind. Electron.*, vol. 56, no. 4, pp. 1101–1108, Apr. 2009.

[12] W. Li, S. He, and S. Yu, "Improving power density of a cantilever piezoelectric power harvester through a curved L-shape proof mass," *IEEE Trans. Ind. Electron.*, vol. 57, no. 3, pp. 868–876, Mar. 2010.

[13] S. Mehraeen, S. Jagannathan, and K. A. Corzine, "Energy harvesting from vibration with alternate scavenging circuitry and tapered cantilever beam," *IEEE Trans. Ind. Electron.*, vol. 57, no. 3, pp. 820–830, Mar. 2010.

[14] *Seiko AGS Quartz/Wachth Product Literature*. [Online]. Available: [http://global.epson.com/company/milestones/19\\_ags.pdf](http://global.epson.com/company/milestones/19_ags.pdf)

[15] *Thermo Life LPTG*. Thermo Life Energy Corp., St. Paul, MN, 2005. [Online]. Available: <http://www.poweredbythermolife.com/>

[16] I. Stark, "Thermal energy harvesting with thermo life," in *Proc. Int. Workshop Wearable Implantable Body Sens. Netw.*, 2006, pp. 19–22.

[17] E. Carlson, K. Strunz, and B. Otis, "20 mV input boost converter for thermoelectric energy harvesting," in *Proc. Symp. VLSI Circuits*, Jun. 2009, pp. 162–163.

[18] A. Nasiri, S. A. Zabalawi, and G. Mandic, "Indoor power harvesting using photovoltaic cells for low-power applications," *IEEE Trans. Ind. Electron.*, vol. 56, no. 11, pp. 4502–4509, Nov. 2009.

[19] T. Celik and H. Kusetogullari, "Solar-powered automated road surveillance systems for speed violation detection," *IEEE Trans. Ind. Electron.*, vol. 57, no. 9, pp. 3216–3227, Sep. 2010.

[20] A. Bertacchini, D. Dondi, L. Larcher, and P. Pavan, "Performance analysis of solar energy harvesting circuits for autonomous sensors," in *Proc. 34th Annu. Conf. IEEE Ind. Electron.*, Nov. 2008, pp. 2655–2660.

[21] T. Sogorb, J. V. Llario, J. Pelegri, R. Lajara, and J. Alberola, "Studying the feasibility of energy harvesting from broadcast RF station for WSN," in *Proc. IEEE Instrum. Meas. Technol. Conf.*, May 2008, pp. 1360–1363.

[22] L. Du, C. Wang, X. Li, L. Yang, Y. Mi, and C. Sun, "A novel power supply of online monitoring systems for power transmissions lines," *IEEE Trans. Ind. Electron.*, vol. 57, no. 8, pp. 2889–2895, Aug. 2010.

[23] N. S. Shenck and J. A. Paradiso, "Energy scavenging with shoe-mounted piezoelectrics," *IEEE Micro*, vol. 21, no. 3, pp. 30–42, May/June 2001.

[24] T. Starner and J. A. Paradiso, "Human-generated power for mobile electronics," in *Low-Power Electronics Design*, C. Piguet, Ed. Boca Raton, FL: CRC Press, 2004, ch. 45, pp. 1–35.

[25] A. Khaligh, Z. Peng, X. Wu, and Y. Xu, "A hybrid energy scavenging topology for human-powered mobile electronics," in *Proc. 34th Annu. Conf. IEEE Ind. Electron.*, Nov. 2008, pp. 448–453.

[26] J. G. Rocha, L. M. Goncalves, P. F. Rocha, M. P. Silva, and S. Lanceros-Mendez, "Energy harvesting from piezoelectric materials fully integrated in footwear," *IEEE Trans. Ind. Electron.*, vol. 57, no. 3, pp. 813–819, Mar. 2010.

[27] *Europractice*. [Online]. Available: <http://www.europractice-ic.com>

[28] *Energy-Harvesting Scheme Targets 'Sustainable' Buildings*. [Online]. Available: <http://www.eetimes.com/conf/electonica/showArticle.jhtml?articleID=212002045&kc=2445>

[29] *Energy Harvesting*, EnOcean GmbH, Oberhaching, Germany. [Online]. Available: <http://www.enocean.com/>

[30] S. Upson, "Putting wireless power to work," *IEEE Spectr.*, vol. 45, no. 6, p. 16, Jun. 2008.

[31] M. Donelan, Q. Li, V. Naing, J. A. Hoffer, D. J. Weber, and A. D. Kuo, "Biomechanical energy harvesting: Generating electricity during walking with minimal user effort," *Science*, vol. 319, no. 5864, pp. 807–810, Feb. 2008.

[32] H.-P. Tan, P. W. Q. Lee, W. K. G. Seah, and Z. A. Eu, "Impact of power control in wireless sensor networks powered by ambient energy harvesting (WSN-HEAP) for railroad health monitoring," in *Proc. Int. Conf. Adv. Inf. Netw. Appl. Workshops*, May 2009, pp. 804–809.

[33] R.-G. Lee, K.-C. Chen, S.-S. Chiang, C.-C. Lai, H.-S. Liu, and M.-S. Wei, "A backup routing with wireless sensor network for bridge monitoring system," in *Proc. 4th Annu. Commun. Netw. Serv. Res. Conf.*, May 2006, pp. 157–161.

[34] *MicroStrain EH-Link Technical Product Overview*, MicroStrain, Inc., Williston, VT, 2009. [Online]. Available: [http://www.microstrain.com/product\\_datasheets/](http://www.microstrain.com/product_datasheets/)

[35] *Midé Engineering Smart Technologies*. Mide Tehnology Corp., Medford, MA. [Online]. Available: <http://www.mide.com/>

[36] *Perpetuum PMG17-100 Data Sheet*, Perpetuum Ltd., Southampton, U.K., 2008. [Online]. Available: <http://www.perpetuum.com/>

[37] *TI CC430 RF SoC Data Sheets*, Analog, Embedded Process., Semicond. Company, Texas Instrum., Dallas, TX, 2010. [Online]. Available: <http://www.ti.com>

[38] A. Khaligh, P. Zheng, and C. Zheng, "Kinetic energy harvesting using piezoelectric and electromagnetic technologies—State of the art," *IEEE Trans. Ind. Electron.*, vol. 57, no. 3, pp. 850–860, Mar. 2010.

[39] M. Ferrari, V. Ferrari, D. Marioli, and A. Taroni, "Modeling, fabrication and performance measurements of a piezoelectric energy converter for power harvesting in autonomous microsystems," *IEEE Trans. Instrum. Meas.*, vol. 55, no. 6, pp. 2096–2101, Dec. 2006.

[40] M. Ferrari, V. Ferrari, M. Guizzetti, and D. Marioli, "An autonomous battery-less sensor module powered by piezoelectric energy harvesting with RF transmission of multiple measurement signals," *Smart Mater. Struct.*, vol. 18, no. 8, pp. 1–9, Aug. 2009.

[41] D. J. de Villiers, S. Kaplan, and R. H. Wilkinson, "Energy harvesting for a condition monitoring mote," in *Proc. 34th Annu. Conf. IEEE Ind. Electron.*, Nov. 2008, pp. 2161–2166.

- [42] V. C. Gungor and G. P. Hancke, "Industrial wireless sensor networks: Challenges, design principles, and technical approaches," *IEEE Trans. Ind. Electron.*, vol. 56, no. 10, pp. 4258–4265, Oct. 2009.
- [43] Y. Ting, G. Hariyanto, B. K. Hou, S. Ricky, S. Amelia, and C.-K. Wang, "Investigation of energy harvest and storage by using curve-shape piezoelectric unimorph," in *Proc. Int. Symp. Ind. Electron.*, Jul. 2009, pp. 2047–2052.
- [44] S. Dwari, R. Dayal, L. Parsa, and K. N. Salama, "Efficient direct ac-to-dc converters for vibration-based low voltage energy harvesting," in *Proc. 34th Annu. Conf. IEEE Ind. Electron.*, Nov. 2008, pp. 2320–2325.
- [45] A. M. Paracha, P. Basset, C. L. P. Lim, F. Marty, P. Poulighet, G. Amendola, and T. Bourounia, "Design and fabrication issues of a silicon-based vibration powered electric energy generator using parallel plate and in-plane mechanism," in *Proc. 32nd Annu. Conf. IEEE Ind. Electron.*, Nov. 2006, pp. 2915–2920.
- [46] A. Ashry, K. Sharaf, and M. Ibrahim, "A simple and accurate model for RFID rectifier," *IEEE Syst. J.*, vol. 2, no. 4, pp. 520–524, Dec. 2008.
- [47] J. P. Curty, N. Joehl, C. Dehollain, and M. Declercq, "Remotely powered addressable UHF RFID integrated system," *IEEE J. Solid-State Circuits*, vol. 40, no. 11, pp. 2193–2202, Nov. 2005.
- [48] Y. Yao, Y. Shi, and F. F. Dai, "A novel low-power input-independent MOS AC/DC charge pump," in *Proc. IEEE Int. Symp. Circuits Syst.*, May 2005, pp. 380–383.
- [49] J. Yi, W. Ki, and C. Tsui, "Analysis and design strategy of UHF micro-power CMOS rectifiers for micro-sensor and RFID applications," *IEEE Trans. Circuits Syst. I, Reg. Papers*, vol. 54, no. 1, pp. 153–166, Jan. 2007.
- [50] E. J. Carlson, K. Strunz, and B. P. Otis, "A 20 mV input boost converter with efficient digital control for thermoelectric energy harvesting," *IEEE J. Solid-State Circuits*, vol. 45, no. 4, pp. 741–750, Apr. 2010.
- [51] I. Doms, P. Merken, C. Van Hoof, and R. P. Mertens, "Capacitive power management circuit for micropower thermoelectric generators with a 1.4  $\mu$ A controller," *IEEE J. Solid-State Circuits*, vol. 44, no. 10, pp. 2824–2833, Oct. 2009.
- [52] C. Van Hoof, V. Leonov, and R. J. M. Vullers, "Thermoelectric and hybrid generators in wearable devices and clothes," in *Proc. 6th Int. Workshop Wearable Implantable Body Sens. Netw.*, Jun. 2009, pp. 195–200.
- [53] E. O. Torres, M. Chen, H. P. Forghani-zadeh, V. Gupta, N. Keskar, L. A. Milner, H.-I. Pan, and G. A. Rincon-Mora, "SiP integration of intelligent, adaptive, self-sustaining power management solutions for portable applications," in *Proc. Int. Symp. Circuits Syst.*, May 2006, pp. 5311–5314.
- [54] CMP-TIMA. [Online]. Available: <http://cmp.imag.fr>
- [55] M. Stordeur and I. Stark, "Low power thermoelectric generator—Self-sufficient energy supply for micro systems," in *Proc. 16th Int. Conf. Thermoelectrics*, 1997, pp. 575–577.
- [56] N. Savage, "Grid on a chip," *IEEE Spectr.*, vol. 46, no. 12, p. 15, Dec. 2009.
- [57] A. Reinders, "Options for photovoltaic solar energy systems in portable products," in *Proc. 4th TCME*, Apr. 2002, pp. 1–13.
- [58] M. A. Green, "Photovoltaics: Technology overview," *Energy Policy*, vol. 28, pp. 989–998, 2000.
- [59] IXYS *Efficiency through Technology*. [Online]. Available: <http://www.ixys.com>
- [60] J. Colomer, J. Brufau, P. Miribel-Catala, A. Saiz-Vela, M. Puig-Vidal, and J. Samitier, "Power conditioning circuitry for a self-powered mobile system based on an array of micro PZT generators in a 0.13  $\mu$ m technology," in *Proc. IEEE Int. Symp. Ind. Electron.*, Jun. 2007, pp. 2353–2357.
- [61] J. Brufau and M. Puig, "Piezoelectric polymer model validation applied to mm size micro-robot I-SWARM (intelligent swarm)," in *Proc. Smart Struct. Mater.*, SPIE, 2006, vol. 6166, pp. 229–240.
- [62] C. Sauer, M. Stanacevic, G. Cauwenberghs, and N. Thakor, "Power harvesting and telemetry in CMOS for implant devices," *IEEE Trans. Circuits Syst. I, Reg. Papers*, vol. 52, no. 12, pp. 2605–2613, Dec. 2005.
- [63] N. Utsuyama, H. Yamaguchi, S. Obara, H. Tanaka, S. Fukuta, J. Nakahira, S. Tanabe, E. Bando, and H. Miyamoto, "Telemetry of human electrocardiograms in aerial and aquatic environments," *IEEE Trans. Biomed. Eng.*, vol. 35, no. 10, pp. 881–884, Oct. 1988.
- [64] J. Van Ham, P. Reynders, and R. Puers, "An autonomous implantable distraction nail controlled by an inductive power and data link," in *Proc. Transducers Eurosensors XXI*, 2007, pp. 427–430.
- [65] Zarlink Semiconductors, Inc. [Online]. Available: [www.zarlink.com](http://www.zarlink.com)
- [66] U. S. Inan and A. S. Inan, *Electromagnetic Waves: Electromagnetic Radiation and Elementary Antennas*. Englewood Cliffs, NJ: Prentice-Hall, 2000.
- [67] L. W. Hart, H. W. Ko, J. H. Meyer, D. P. Vasholz, and R. I. Joseph, "A noninvasive electromagnetic conductivity sensor for biomedical applications," *IEEE Trans. Biomed. Eng.*, vol. 35, no. 12, pp. 1011–1022, Dec. 1988.
- [68] E. S. Hochmair, "System optimization for improved accuracy in transcutaneous signal and power transmission," *IEEE Trans. Biomed. Eng.*, vol. BME-31, no. 2, pp. 177–186, Feb. 1984.
- [69] K. Van Schuylenbergh and R. Puers, *Inductive Powering. Basic Theory and Application to Biomedical Systems*. New York: Springer-Verlag, 2009.
- [70] G. A. Elliott, S. Raade, G. A. Covic, and J. T. Boys, "Multi-phase pickups for large lateral tolerance contactless power-transfer systems," *IEEE Trans. Ind. Electron.*, vol. 57, no. 5, pp. 1590–1599, May 2010.
- [71] A. J. Moradewicz and M. P. Kazmierkowski, "Contactless energy transfer system with FPGA-controlled resonant converter," *IEEE Trans. Ind. Electron.*, vol. 57, no. 9, pp. 3181–3190, Sep. 2010.
- [72] J. Colomer-Farrarons, P. Miribel-Català, I. Rodríguez, and J. Samitier, "CMOS front-end architecture for in-vivo biomedical implantable devices," in *Proc. 35th Annu. Conf. IEEE Ind. Electron.*, Nov. 3–5, 2009, pp. 4437–4444.
- [73] B. Lenaerts and R. Puers, *Omnidirectional Inductive Powering for Biomedical Implants*. New York: Springer-Verlag, 2009.
- [74] M. Soma, D. C. Galbraith, and R. L. White, "Radio-frequency coils in implantable devices: Misalignment analysis and design procedure," *IEEE Trans. Biomed. Eng.*, vol. 34, no. 4, pp. 276–282, Apr. 1987.
- [75] Microchip Application Note, Antenna Circuit Design for RFID Application, AN710, 2003.
- [76] *ST Microelectronics Application Note, Antenna (and Associated Components) Matching—Circuit Calculation for the CRX14 Coupler*, AN1806, Feb. 2006.
- [77] S. S. Basat, K. Lim, J. Laskar, and M. Tentzeris, "Design and modelling of embedded 13.56 MHz RFID antennas," in *Proc. IEEE Antennas Propag. Soc. Int. Symp.*, Jul. 2005, vol. 4B, pp. 64–67.
- [78] *TRF7960 Multi-Standard Fully Integrated 13.56-MHz RFID Analog Front End*, Analog, Embedded Process., Semicond. Company, Texas Instrum., Dallas, TX, 2010. [Online]. Available: <http://focus.ti.com/docs/prod/folders/print/trf7960.html>
- [79] Y. Zhu, S. O. R. Moheimani, and M. R. Yuce, "Ultrasonic energy transmission and conversion using a 2-D MEMS resonator," *IEEE Electron Device Lett.*, vol. 31, no. 4, pp. 374–376, Apr. 2010.
- [80] A. J. Cardoso, C. R. Rodrigues, R. S. Pippi, C. A. Prior, and F. C. B. Vieira, "CMOS energy harvester based on a low-cost piezoelectric acoustic transducer," in *Proc. 49th IEEE Int. Midwest Symp. Circuits Syst.*, Aug. 2006, vol. 1, pp. 70–74.
- [81] M. H. Cheng and Z. W. Wu, "Low-power low-voltage reference using peaking current mirror circuit," *Electron. Lett.*, vol. 41, no. 10, pp. 572–573, May 2005.
- [82] G. Giustolisi, G. Palumbo, M. Criscione, and F. Cutri, "A low-voltage low-power voltage reference based on subthreshold MOSFET's," *IEEE J. Solid-State Circuits*, vol. 38, no. 1, pp. 151–154, Jan. 2003.
- [83] M. D. Ker and J. S. Chen, "New curvature-compensation technique for CMOS bandgap reference with sub-1-V operation," *IEEE Trans. Circuits Syst. II, Exp. Briefs*, vol. 53, no. 8, pp. 667–671, Aug. 2006.
- [84] K. Sanborn, D. Ma, and V. Ivanov, "A sub-1-V low-noise bandgap voltage reference," *IEEE J. Solid-State Circuits*, vol. 42, no. 11, pp. 2466–2481, Nov. 2007.
- [85] J. Colomer-Farrarons, P. Miribel-Catala, A. Saiz-Vela, M. Puig-Vidal, and J. Samitier, "Power-conditioning circuitry for a self-powered system based on micro PZT generators in a 0.13  $\mu$ m low-voltage low-power technology," *IEEE Trans. Ind. Electron.*, vol. 55, no. 9, pp. 3249–3257, Sep. 2008.
- [86] R. Tantawy and E. J. Brauer, "Performance evaluation of CMOS low dropout voltage regulators," in *Proc. 47th IEEE Int. Midwest Symp. Circuits Syst.*, 2004, pp. 1–141–1–144.
- [87] *LP2985 Datasheet*, Analog, Embedded Process., Semicond. Company, Texas Instrum., Dallas, TX, Jun. 2001. [Online]. Available: <http://www.ti.com>
- [88] K. N. Leung, P. K. T. Mok, and S. K. Lau, "A low-voltage CMOS low-dropout regulator with enhanced loop response," in *Proc. Int. Symp. Circuits Syst.*, 2004, pp. 385–388.
- [89] *SLYT194 Datasheet*, Analog, Embedded Process., Semicond. Company, Texas Instrum., Dallas, TX, 1999. [Online]. Available: <http://www.ti.com>
- [90] T. Paing, J. Shin, R. Zane, and Z. Popovic, "Resistor emulation approach to low-power RF energy harvesting," *IEEE Trans. Power Electron.*, vol. 23, no. 3, pp. 1494–1501, May 2008.
- [91] V. Pop, J. Penders, R. van Schaijk, and R. Vullers, "The limits and challenges for power optimization and system integration in state-of-the-art

wireless autonomous transducer solutions,” in *Proc. 3rd Eur. Conf. Smart Syst. Integr.*, Mar. 2009, pp. 544–547.

- [92] T. Torfs, V. Leonov, C. van Hoof, and B. Gyselinckx, “Body-heat powered autonomous pulse oximeter,” in *Proc. 5th IEEE Conf. Sens.*, 2006, pp. 427–430.
- [93] L. Huang, M. Ashouei, F. Yazicioglu, J. Penders, R. Vullers, G. Dolmans, P. Merken, J. Huisken, H. de Groot, C. von Hoof, and B. Gyselinckx, “Ultra-low power sensor design for wireless body area networks: Challenges, potential solutions, and applications,” *Int. J. Digital Content Technol. Appl.*, vol. 3, no. 3, pp. 136–148, Sep. 2009.



**J. Colomer-Farrarons** (S'06) received the B.Sc. degree in electrical engineering from Salesians Technical Engineering School, Escola Universitària Salesiana de Sarrià, Barcelona, Spain, in 2002 and the M.Sc. degree in electrical engineering and the Ph.D. degree from the University of Barcelona, Barcelona, in 2005 and 2010, respectively.

From 2002 to 2005, he was a Hardware Design Engineer with the automotive company Francisco Alberó, S.A. Since 2005, he has been a Research Fellow with the SIC-BIO: Bioelectronics and Nanobioengineering Laboratory, Department of Electronics, University of Barcelona, working on low-voltage low-power circuits, smart power circuits, harvesting design circuits, interface circuits for biomedical applications, and microelectronic design.



**P. Miribel-Català** (M'08) received the M.Sc. degree in physics and the Ph.D. degree from the University of Barcelona, Barcelona, Spain, in 1994 and 2000, respectively.

From 1993 to 1999, he was a Research Fellow with the Systems for Instrumentation and Communications Laboratory (SIC Laboratory), University of Barcelona, working on high-voltage smart power circuits and microelectronic design. In 1998, he was a Visiting Research Fellow with the Laboratoire d'Analyse et d'Architecture des Systèmes, Centre National de la Recherche Scientifique, Toulouse, France. During a postdoctoral stage, he was with the design center of ON semiconductor Inc., Toulouse, working on designing power management integrated dc–dc converters. Since 2003, he has been an Associate Professor (Professor Titular) with the SIC-BIO: Bioelectronics and Nanobioengineering Laboratory, Department of Electronics, University of Barcelona. His research topics are focused on low-voltage low-power integrated circuits, interface and analog processing circuits, particularly for biomedical applications, and smart power and power management circuits.



**A. Saiz-Vela** (S'06) received the M.Sc. degree in electrical engineering from the University of Barcelona, Barcelona, Spain, in 2001, where he is currently working toward the Ph.D. degree in electrical engineering in the VLSI design group of the SIC-BIO: Bioelectronics and Nanobioengineering Laboratory.

From 2001 to 2003, he was a Hardware Design Engineer with the research division of Comelta, AMR Systems, and Sony (Plasma TV design group, Sony BCN Tech. Center, Barcelona). His main research interests include efficient high-voltage switched-capacitor dc–dc converter design (commonly known as charge pumps), numerical simulation of analog circuits, and analog driving circuit design for PZT-based actuators in miniaturized systems (specifically miniaturized robots).



**J. Samitier** (M'95) received the B.S. degree in physics and the Ph.D. degree from the University of Barcelona, Barcelona, Spain, in 1982 and 1986, respectively.

From February 1984 to June 1985, he was a Visiting Research Fellow with the Philips Electronic Laboratory (LEP), Paris, France. From March 2001 to June 2005, he was the Director of the Department of Electronics and the Deputy Head of the Barcelona Science Park (PCB), University of Barcelona. He is currently a full Professor with the Department of Electronics, University of Barcelona, and the Director of the Nanobioengineering Laboratory supported by the Institute of Bioengineering of Catalonia (IBEC). He is the Coordinator of the SIC-BIO: Bioelectronics and Nanobioengineering Laboratory and of the Spanish Platform on Nanomedicine and a Member of the nanotechnology networks: NanoSpain, European network Phantom, and Nano2life European Network of Excellence. In the last fifteen years, he has participated and coordinated several European projects concerning integrated microsystems and, more recently, nanotechnology devices. He has published more than 150 scientific papers in these fields and is the holder of four licensed patents. His current research and developed projects concern the development of nanotechnologies for biomedical applications.

Dr. Samitier received the Barcelona City Prize in the area of technology from the Barcelona City Council in 2003.